IJMMM International Journal of Minerals, Metallurgy and Materials 矿物冶金与材料学报（英文版）

Enhanced recovery of high-purity Fe powder from iron-rich electrolytic manganese residue by slurry electrolysis

Wenxing Cao, Jiancheng Shu, Jiaming Chen, Zihan Li, Songshan Zhou, Shushu Liao, Mengjun Chen, and Yong Yang

Cite this article as:
Wenxing Cao, Jiancheng Shu, Jiaming Chen, Zihan Li, Songshan Zhou, Shushu Liao, Mengjun Chen, and Yong Yang, Enhanced recovery of high-purity Fe powder from iron-rich electrolytic manganese residue by slurry electrolysis, *Int. J. Miner. Metall. Mater.*, 31(2024), No. 3, pp. 531-538. https://doi.org/10.1007/s12613-023-2729-z

---

INTERNATIONAL JOURNAL OF
Minerals, Metallurgy and Materials

Volume 31, Number 3, March 2024
Page 531

Research Article https://doi.org/10.1007/s12613-023-2729-z

Enhanced recovery of high-purity Fe powder from iron-rich electrolytic manganese residue by slurry electrolysis

Wenxing Cao[1)], *Jiancheng Shu*[1),✉], *Jiaming Chen*[1)], *Zihan Li*[1)], *Songshan Zhou*[1)], *Shushu Liao*[1)], *Mengjun Chen*[1)], *and Yong Yang*[2,3)]

1) Key Laboratory of Solid Waste Treatment and Resource Recycle (SWUST), Ministry of Education, Southwest University of Science and Technology, Mianyang 621010, China

2) School of Chemistry and Chemical Engineering, Chongqing University, Chongqing 400044, China

3) Daxin Manganese Mining Branch of South Manganese Group Limited, Chongzuo 532315, China

(Received: 19 May 2023; revised: 15 August 2023; accepted: 16 August 2023)

Abstract: Iron-rich electrolytic manganese residue (IREMR) is an industrial waste produced during the processing of electrolytic metal manganese, and it contains certain amounts of Fe and Mn resources and other heavy metals. In this study, the slurry electrolysis technique was used to recover high-purity Fe powder from IREMR. The effects of IREMR and H_2SO_4 mass ratio, current density, reaction temperature, and electrolytic time on the leaching and current efficiencies of Fe were studied. According to the results, high-purity Fe powder can be recovered from the cathode plate, and the slurry electrolyte can be recycled. The leaching efficiency, current efficiency, and purity of Fe reached 92.58%, 80.65%, and 98.72wt%, respectively, at a 1:2.5 mass ratio of H_2SO_4 and IREMR, reaction temperature of 60°C, electric current density of 30 mA/cm^2, and reaction time of 8 h. In addition, vibrating sample magnetometer (VSM) analysis showed that the coercivity of electrolytic iron powder was 54.5 A/m, which reached the advanced magnetic grade of electrical pure-iron powder (DT4A coercivity standard). The slurry electrolytic method provides fundamental support for the industrial application of Fe resource recovery in IRMER.

Keywords: iron-rich electrolytic manganese residue; slurry electrolysis; high-purity iron powder; leaching efficiency; current efficiency

1. Introduction

Manganese is an important metallurgical and chemical raw material with applications in various fields, including metallurgy, chemistry, batteries, fertilizer, and feed additives [1–2]. Currently, manganese is mainly obtained from low-iron manganese ores through electrolytic methods [3–4]. With the depletion of traditional low-iron manganese ore resources, the utilization of plentiful high-iron manganese ores in the manufacture of electrolytic manganese metal is gradually expanding [5–6], expected to produce a huge amount of iron-rich electrolytic manganese residue (IREMR).

Compared with traditional electrolytic manganese residue, IREMR contains more Fe (20wt%–45wt%), Mn (8wt%–10wt%), and other heavy metals and thus can pose more harm to the environment [7–10]. The annual emission of IREMR in China is approximately 15–30 kt [10–12]. At present, the primary use of IREMR is in the preparation of desulfurizers and cement correction agents, but its utilization is low; in addition, most IREMR is still disposed of by direct storage [13–14]. The large amount of IREMR not only pollutes the environment [8] but also wastes valuable resources, such as soluble Fe and Mn. Therefore, a new method must be developed for the resource utilization of IREMR for electrolytic manganese enterprises [15].

Slurry electrolysis is a hydrometallurgical process that combines metal dissolution, electrolyte depuration, and electrowinning in a single reactor, and it has attracted extensive attention from researchers because of its environmental friendliness and short procedure [16–18]. High-purity Fe powder can be obtained using the electrolytic method [19], and this material is widely used in soft magnetic materials because of its good ductility, soft magnetic properties, thermal properties, electrical conductivity, and corrosion resistance [20–25]. Previously, our research team used the slurry electrolysis method to recover Cu from waste printed circuit boards; the recovery efficiency and purity of Cu were higher than 90% and 99%, respectively [16,26]. Furthermore, an escalation experiment with a 5 L scale was conducted, and the results confirmed the feasibility of such a method for use in the industry, given its similar findings at the laboratory scale [27]. In addition, most slurry electrolysis systems adopted for valuable-metal recovery are acidic because of their high recovery efficiency and strong adaptability to such a complex system [16–17]. Therefore, the recovery of high-purity Fe powder from IREMR via slurry electrolysis is fully feasible.

✉ Corresponding author: Jiancheng Shu E-mail: sjcees@126.com

This study proposes a novel and efficient acidic slurry electrolysis system made of IREMR–H_2O–H_2SO_4–Fe for the recovery of Fe from IREMR. H_2SO_4 can provide a stable electrolytic condition and offer an environment that favors dissolution of IRMER [28–30], and the addition of reduced Fe can provide sufficient Fe^{2+}. The effects of reaction temperature, H_2SO_4 and IREMR mass ratio, electrolytic time, and current density on the leaching and recovery efficiencies of Fe are discussed here in detail.

2. Experimental

2.1. Materials

The IREMR was dried at 60°C for 24 h at a steady weight before being passed through the sieve mesh with a diameter of 0.25 mm [31]. Table 1 shows the main chemical composition of IREMR. The chemical reagents utilized in this study, namely, H_2SO_4 and reduced Fe powder, were analytically pure and used without further purification. A cube electrolytic cell, which had a capacity of 504 mL (12 cm × 7 cm × 6 cm) and was made of polytetrafluoroethylene, was used in the experiment. The anode and cathode plates adopted a dimensionally stable anode of ruthenium–titanium plate and a stainless steel plate, respectively. A direct current power supply (JB-500, Jiangbo, Shenzhen, China) was used for the current supply, and a water bath (FD-101S, Shanghai, China) was used to control the temperature of the slurry electrolysis reaction.

Table 1. XRF analysis of IREMR wt%

Fe_2O_3	SO_3	MnO	SiO_2	CaO	Al_2O_3	MgO	Other
44.30	24.43	8.84	8.25	4.78	4.71	2.98	1.71

2.2. Process

After pretreatment, 50 g IREMR was added to the anode chamber of the electrolytic cell, and the anode and cathode poles were separated using a double layer of acid–alkali-resistant filter cloth. Deionized water was added to the anode chamber at a solid–liquid ratio of 1:5 to create a slurry. Next, certain amounts of H_2SO_4 and reduced Fe powder were added to the anode chamber, and the amount of reduced Fe added was the finding of theoretical calculations and practical experiments. The mass ratio of reduced Fe and IREMR was 1:7. Then switch on the anode and cathode power supply. The effects of temperature (30–70°C), mass ratio of H_2SO_4 to IREMR (1:10–1:2), current density (10–50 mA/cm^2), and electrolytic time (4–12 h) on the leaching and current efficiencies of Fe were investigated. The cathode products were collected after each run, and their purity was tested and characterized. Using Eq. (1), the leaching efficiency of metal elements was determined:

$$\mu = \frac{V \cdot C}{M \cdot W} \tag{1}$$

where μ refers to the metal leaching efficiency, V indicates the volume of the leaching solution (L), C represents the concentration of elements in the leaching solution (mg/L), M denotes the mass of the sample before leaching (g), and W is the mass fraction of elements in the sample before leaching [31–32].

The current efficiency was calculated using Eq. (2):

$$\eta = \frac{m}{I \cdot t \cdot k} \tag{2}$$

where η indicates the current efficiency, m denotes the actual product quality on the cathode plate (g), I refers to the constant current intensity (A), t is the time of electrolysis (h), and k represents the electrochemical equivalent ($g \cdot A^{-1} \cdot h^{-1}$) [26,33]. The calculation results of leaching and current efficiencies were averaged over three parallel tests.

2.3. Analytical methods

Inductively coupled plasma emission spectrometry (ICP-OES; Thermo Fisher Scientific, ICAP 6500, USA) was used to analyze heavy-metal concentrations in IREMR and the leached IREMR. The chemical composition of IREMR was examined using X-ray fluorescence spectrometry (XRF; PANalytical B.V., Axios, The Netherlands). An X-ray diffractometer (XRD; Ultima IV, Rigaku/Japan) was employed to examine the chemical phases of IREMR. Scanning electron microscopy (SEM; Slgma 300, Germany) was utilized to determine the surface morphology of IREMR and leached IREMR. Energy dispersive spectrometer (EDS; Oxford x-max, America) was used for the surface element content analysis of IREMR and leached IREMR. The Fourier transform infrared spectroscopy (FT-IR) of the samples were obtained using a Magna 550II FT-IR spectrometer (PerkinElmer Frontier, America) via the KBr pellet method. X-ray photoelectron spectroscopy (XPS; Thermo Scientific K-Alpha, America) analysis was conducted on precipitated substances from the cathode, it was also used to fit the peak position and calibrate the valence state of electrolytic Fe powder precipitated from the cathode. A vibrating sample magnetometer (VSM; LakeShore-7404, America) was conducted to measure the soft magnetic properties of the electrolytic Fe powder. An electrochemical workstation (CHI660D, China) was used to produce the cyclic voltammetry (CV) curve of mineral grout.

3. Results and discussion

3.1. Effect of temperature

As shown in Fig. 1, the leaching efficiency of Fe and current efficiency increased gradually with the increase in temperature, and at 60°C, the leaching efficiency of Fe and current efficiency reached as high as was 78.81%, and the current efficiency reached a maximum of 60.35%, respectively. When the temperature continues to rise beyond 60°C, the leaching efficiency was only with a slight increase, but the current efficiency was with an obviously decrease. This is because as the temperature increased, the slurry exhibited a decreased viscosity and an increased diffusion rate, which promoted the leaching of Fe from IREMR. Besides, the current efficiency of Fe also increased with the increase in the leaching efficiency of Fe. However, at temperatures greater than

60°C, the leaching efficiency of Fe in IREMR almost reached saturation, and the resistance of the slurry increased with the increase in the temperature, which led to a decreased current efficiency [34]. Furthermore, as the increase in temperature accelerated the consumption of H^+ in the slurry, its final pH increased with the increase in the temperature. The pH of the slurry in the cathode chamber was consistently higher than that in the anode chamber. In consideration of the current efficiency of Fe, the optimal temperature for the subsequent experiments was 60°C.

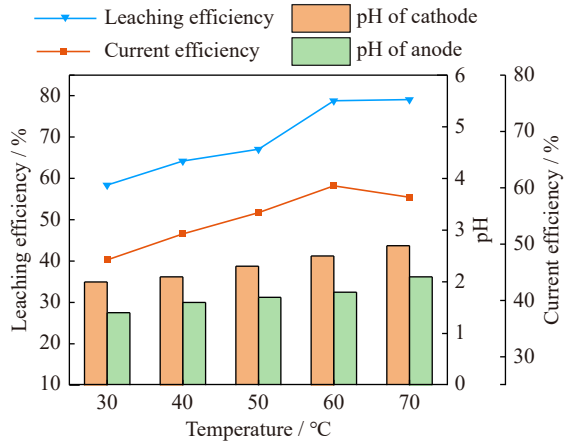

Fig. 1. Effect of temperature on the leaching and current efficiencies of Fe (H_2SO_4 and IREMR mass ratio: 1:3.3; current density: 30 mA/cm^2; electrolytic time: 4 h).

3.2. Effect of H_2SO_4 and IREMR mass ratio

When the mass ratio of H_2SO_4 to IREMR reached 1:2.5, the leaching efficiency of Fe was 92.43%, and the current efficiency reached a maximum value of 69.71% (Fig. 2). However, when the proportion of H_2SO_4 to IREMR increased continuously, the leaching efficiency of Fe increased slowly, and the current efficiency decreased. The primary reason for this finding was as follows. The increased addition of H_2SO_4 promoted the leaching of Fe from IREMR, and the current efficiency increased as the Fe in IREMR was being leached out. However, at the H_2SO_4 to IREMR mass ratio of 1:2.5, the leaching of IREMR reached saturation, and H_2SO_4 continuously reduced the pH of the slurry, which was not conducive to the reduction of Fe^{3+} and the electric deposition of cathode high-purity Fe powder; as a result, the current efficiency decreased [6,35]. The final pH of the slurry decreased with the increase in H_2SO_4 addition, with the slurry in the cathode chamber exhibiting a constantly higher pH than that in the anode chamber. In consideration of the current efficiency factor, the 1:2.5 mass ratio of H_2SO_4 and IREMR addition was used in the subsequent experiments.

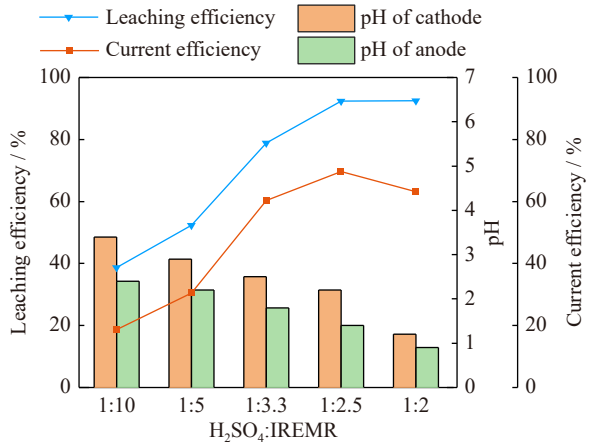

Fig. 2. Effect of mass ratio of H_2SO_4 to IREMR (H_2SO_4 : IREMR) on the leaching and current efficiencies of Fe (temperature: 60°C; current density: 30 mA/cm^2; electrolytic time: 4 h).

3.3. Effect of current density

Fig. 3 shows that the current efficiency of Fe increased with the increase in the current density before the current density was set to 30 mA/cm^2. At the current density of 30 mA/cm^2, the leaching efficiency of Fe was 92.43%, and its maximum current efficiency was 69.71%. The increased current density contributed to the rate of movement of Fe^{2+} from the slurry to the cathode. This condition increased the concentration of Fe^{2+} in the cathode chamber and accelerated the rate of electrodeposition of Fe, which resulted in improved current efficiency. However, the current efficiency decreased at current densities over 30 mA/cm^2, and this phenomenon depended on the current efficiency calculation formula, as shown in Eq. (2). If the other values were constant, the current efficiency decreased with the increase in the current density. The change in current density had minimal effect on the final pH of the slurry. The results showed that the current density of 30 mA/cm^2 favored the electrodeposition of Fe^{2+} into electrolytic Fe powder in the slurry. Thus, in the subsequent experiments, a current density of 30 mA/cm^2 was used.

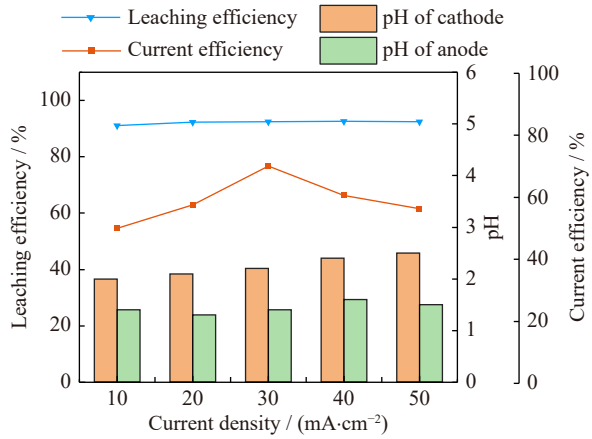

Fig. 3. Effect of current density on the leaching and current efficiencies of Fe (temperature: 60°C; H_2SO_4 and IREMR mass ratio: 1:2.5; electrolytic time: 4 h).

3.4. Effect of electrolytic time

As presented in Fig. 4, the leaching efficiency of Fe almost reached saturation at 4 h of electrolysis, and the current efficiency improved initially and subsequently dropped with the increase in the electrolytic time. When the electrolytic

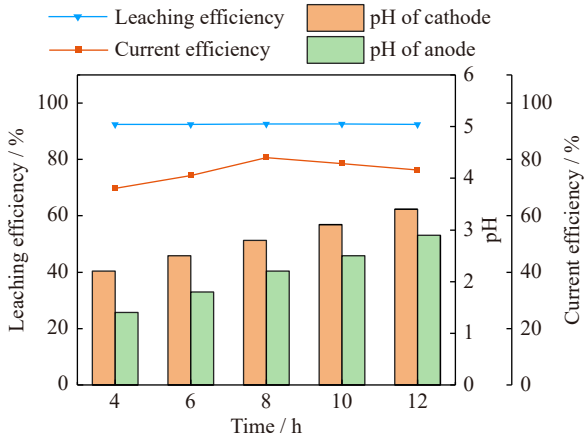

Fig. 4. Effect of electrolytic time on the leaching and current efficiencies of Fe (temperature: 60°C; H_2SO_4 and IREMR mass ratio: 1:2.5; current density: 30 mA/cm^2).

time was set to 8 h, the leaching efficiency of Fe was 92.58%, and the current efficiency of Fe reached the maximum value of 80.65%, and beyond 8 h, the current efficiency decreased, although the Fe powder remained deposited on the cathode plate. Over time, the electrolytic dominance of Fe^{2+} in the slurry gradually changed to H^+, and the final pH of the slurry increased with the increase in electrolytic time. In addition, the pH of the slurry in the cathode chamber was consistently higher than that in the anode chamber. After comprehensive consideration, the best electrolytic time was set to 8 h.

3.5. Leaching and recovery mechanisms of Fe

The tests in Tables 2–4 were performed under optimal conditions with a 1:2.5 mass ratio of H_2SO_4 and IREMR, reaction temperature of 60°C, electric current density of 30 mA/cm^2, and reaction time of 8 h. Tables 1 and 2 show the chemical analysis of IREMR and leached IREMR via XRF. The main chemical components of IREMR included Fe_2O_3, SO_3, MnO, SiO_2, CaO, and Al_2O_3, which accounted for 44.30wt%, 24.43wt%, 8.84wt%, 8.25wt%, 4.78wt%, and 4.71wt%, respectively. The comparison of the content of the chemical component of IREMR and leached IREMR shows that after slurry electrolysis, IREMR metal components, such as Fe_2O_3 and MnO, were leached, and the percentage contents of Fe_2O_3, MnO, and MgO in the leached IREMR decreased to 8.73wt%, 0.66wt%, and 0.82wt%, respectively. Correspondingly, the percentages of elements that were not leached increased. Table 3 shows the results of the quantitative analysis of IREMR and leached IREMR obtained by ICP-OES after digestion in accordance with HJ 832-2017, which accurately tested the contents of metallic elements in IREMR and leached IRMER. As displayed in Table 3, the contents of Mn, Fe, Ca, Mg, and Al in the IREMR were 60.71, 378.52, 39.12, 21.47, and 26.81 mg/g, respectively. Meanwhile, the contents of Mn, Fe, Ca, Mg, and Al in the leached IREMR reached 6.53, 65.69, 89.53, 4.73, and 59.47 mg/g, respectively. These results were consistent with those of the XRF test and showed that H_2SO_4 can enhance the leaching of metals (Mn, Fe, and Mg) in IREMR. Table 4 reveals that the contents of Mn and Fe in the electrolyte, which can be utilized as an electrolytic Fe circulating liquid, after slurry electrolysis were 10.16 and 14.35 g/L, respectively. An ICP test was performed on the electrolytic Fe precipitated from the cathode after digestion, and the results are shown in Table 5 The electrolytic Fe obtained had a purity of 98.72wt%.

Table 2. XRF analysis leached IREMR wt%

Fe_2O_3	SO_3	MnO	SiO_2	CaO	Al_2O_3	MgO	Other
8.73	29.64	0.66	27.88	13.74	14.22	0.82	4.31

Table 3. Chemical composition of IREMR and leached IREMR obtained by ICP-OES in accordance with HJ 832-2017 (mg·g^{-1})

Sample	Mn	Fe	Ca	Mg	Al	Zn	Pd	Cd	Ti	Ni
IREMR	60.71	378.52	39.12	21.47	26.81	0.52	/	4.67	0.17	/
Leached IREMR	6.53	65.69	89.53	4.73	59.47	/	0.01	/	0.37	0.02

Note: "/"—Less than the measured value of the instrument.

Table 4. Chemical composition of electrolyte obtained by ICP-OES (g·L^{-1})

Mn	Fe	Ca	Mg	Al	Zn	Pd	Cd	Ti	Ni
10.16	14.35	0.01	2.69	0.16	0.10	0.32	0.87	0.01	/

Note: "/" —Less than the measured value of the instrument.

Table 5. Chemical composition of cathode electrodeposition samples wt%

Fe	Mn	Mg	Zn	Se	As	Other
98.72	0.76	0.23	0.10	0.01	0.01	0.17

As shown in Fig. 5, the main phase components of IREMR were $(NH_4)_2Fe(SO_4)_2{\cdot}6(H_2O)$ (ammonium jarosite), $CaSO_4{\cdot}2H_2O$ (gypsum), $(NH_4)_2Mg(SO_4)_2{\cdot}6(H_2O)$ (boussingaultite), $(NH_4)_3Al(SO_4)_3$ (aluminum ammonium sulfate), $(Mn,Ca)Mn_4O_9{\cdot}3H_2O$ (rancieite), $Fe(OH)_3$ (iron hydroxide), FeO(OH) (goethite), and SiO_2 (quartz). Then after leached, the phases of $(NH_4)_2Fe(SO_4)_2{\cdot}6(H_2O)$, $(NH_4)_2Mg(SO_4)_2{\cdot}6(H_2O)$, $(NH_4)_3Al(SO_4)_3$, $(Mn,Ca)Mn_4O_9{\cdot}3H_2O$ (rancieite), FeO(OH), and $Fe(OH)_3$ disappeared, and new phases of $(NH_4)Fe_3(SO_4)_2{\cdot}6(H_2O)$, $Al_2(SO_4)_3$, and $Fe_2O_3{\cdot}H_2O$ appeared in the leached IREMR. Thus, the IREMR started to interact with H_2SO_4 and reduced Fe powder to create a new phase. The following are some of the potential reaction equations [36–39]:

$$(NH_4)_2Fe(SO_4)_2{\cdot}6(H_2O) \rightarrow 2NH_4^+ + Fe^{2+} + 2SO_4^{2-} + 6H_2O \quad (3)$$

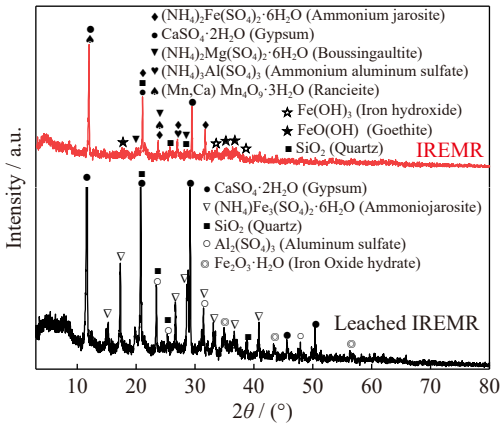

Fig. 5. XRD patterns of IREMR and leached IREMR (temperature: 60°C, H_2SO_4 and IREMR mass ratio: 1:2.5; current density: 30 mA/cm^2; electrolytic time: 8 h).

$$Fe + H_2SO_4 \rightarrow FeSO_4 + H_2 \uparrow \quad (4)$$

$$2Fe(OH)_3 + 3H_2SO_4 \rightarrow Fe_2(SO_4)_3 + 6H_2O \quad (5)$$

$$2Fe^{3+} + Fe \rightarrow 3Fe^{2+} \quad (6)$$

$$Fe^{2+} + 2e^- \rightarrow Fe \quad (7)$$

$$Mn^{2+} + 2e^- \rightarrow Mn \quad (8)$$

$$(NH_4)_2Mg(SO_4)_2·6(H_2O) \rightarrow 2NH_4^+ + Mg^{2+} + 2SO_4^{2-} + 6H_2O \quad (9)$$

As shown in Fig. 6(a), the SEM images recorded at high magnification clearly revealed the presence of irregular clusters in IREMR. EDS analysis revealed that S, O, Mn, and Fe were distributed mainly on the surface of irregular clusters in IREMR, with contents of 3.66wt%, 40.7wt%, 4.15wt%,

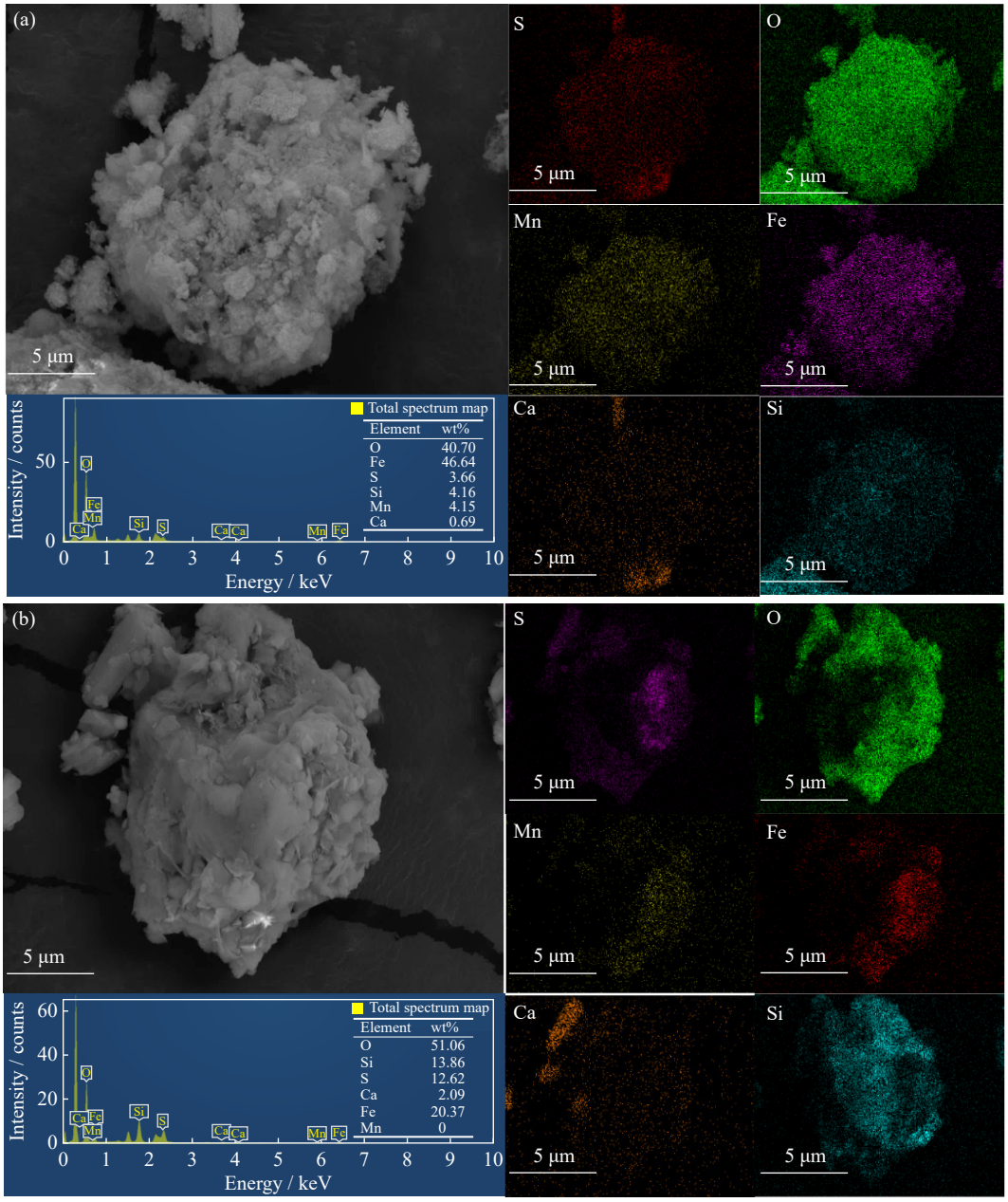

Fig. 6. SEM and EDS diagrams of (a) IREMR and (b) leached IREMR (temperature: 60°C, H_2SO_4 and IREMR mass ratio: 1:2.5; current density: 30 mA/cm^2; electrolytic time: 8 h).

and 46.64wt%, respectively. Fig. 6(b) illustrates that after slurry electrolysis, the clusters exhibited a smoother surface, their morphology did not change drastically, and the contents of S, O, Mn, and Fe were 12.62wt%, 51.06wt%, 0wt%, and 20.37wt%, respectively. Furthermore, according to the comparison of the color depths of Fe and Mn in the EDS spectra of IREMR and leached IREMR, compared with the original IREMR, the colors of Fe and Mn in the leached IREMR were lighter, and the contents of Fe and Mn on the surface were considerably lower, which indicates that H_2SO_4 had a substantial effect on the surface of IREMR, and Fe in IREMR was leached.

As displayed in Fig. 7(a) and (b), the broad peak at 3406 cm^{-1} was the distinctive strips of crystal water, which may be explained by the numerous stretching vibrations of –OH, which indicates the presence of bound water molecules. In addition, at 534 and 604 cm^{-1}, the stretching vibrations of Si–O–Si were visible. The peaks at 1427, 1431, 1008, 1110, 472, and 470 cm^{-1} were characteristic of SO_4^{2-}. In Fig. 7(a), the peak at 1624 cm^{-1} was characteristic of ammonium jarosite minerals [40–41]. The findings demonstrated that the bending vibrations of Fe–OH vanished, and small changes occurred on the vibrational bands of SO_4^{2-} and Si–O–Si. This result indicated that the minerals involving Fe in IREMR were dissolved via acid leaching, and H_2SO_4 had a minimal effect on $CaSO_4{\cdot}2H_2O$ and SiO_2 in IREMR.

Alternating redox reactions at the electrodes were recorded on the CV curve, and the saturated calomel electrode was added as a reference electrode in the original electrolytic system for the CV test. As shown in Fig. 8, a gentle upward current crest band appeared from −0.75 to −0.25 V, and bubble generation was observed at the working electrode, which indicated the occurrence of hydrogen evolution at this voltage. In the forward scanning process, a current spike peak was generated at the electrode potential of 0.84 V, and it corresponded to the dissolution of Fe. A current peak with a sudden drop was generated near the electrode potential of −0.107 V in the reverse scanning process. Meanwhile, a layer of black material attached to the working electrode surface indicated the occurrence of a Fe^{2+} electrodeposition reaction.

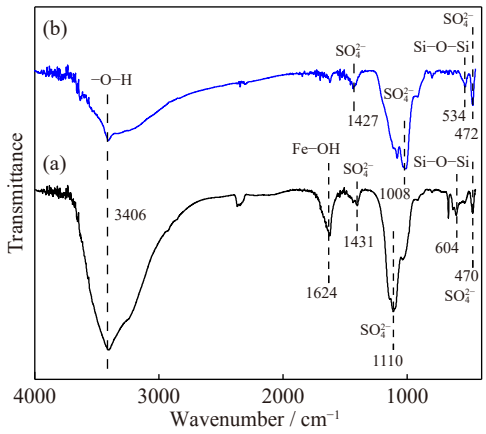

Fig. 7. FT-IR spectra of (a) IREMR and (b) leached IREMR (temperature: 60°C, H_2SO_4 and IREMR mass ratio: 1:2.5; current density: 30 mA/cm^2; electrolytic time: 8 h).

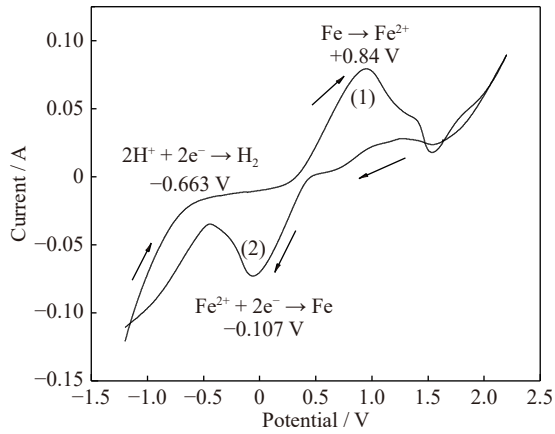

Fig. 8. CV curve of slurry (temperature: 60°C; H_2SO_4 and IREMR mass ratio: 1:2.5).

CV analysis confirmed that the electrode potential of the Fe^{2+} electrodeposition reaction greatly exceeded the H_2 evolution reaction onset potential, and the severe competition between H_2 evolution and Fe^{2+} reduction was one of the reasons for the decrease in current efficiency [17,36].

Fig. 9(a) shows that Fe was the major phase in the electrowinning sample, and the other trace of impurities existed in amorphous form. SEM analysis revealed that the morphology of electrolytic Fe was mainly a stack of cluster-shaped particles (Fig. 9(b)). Fig. 9(c) displays the XPS spectrum of the sample, which contained Fe, Mn, and Mg, specifically the mixing of the electrolytic Fe with Mn and Mg. The peak at 530 eV was attributed to lattice O, which indicates that O^{2-} mostly interacted with Fe to form Fe oxide [31]. As presented in Fig. 9(d), the Fe and Fe^{3+} peaks were located at 710.60 and 713.642 eV, respectively, which meant that some Fe was oxidized after contacting oxygen. These results were consistent with those of XRD and ICP-OES. The VSM analysis showed that the coercivity of the electrolytic Fe powder was 54.5 A/m (Fig. 9(e)), which reached the electrically pure Fe coercivity advanced magnetic grade, and conformed to the DT4A coercivity standard. Fig. 9(f) and (g) shows the TEM micrographs of the electrowinning sample. The high-resolution image of the electrowinning sample revealed its crystalline structure. The exfoliated electrolytic Fe (Fig. 9(f)) presented ordered lattice fringes with a *d*-spacing of approximately 1.018 nm, which corresponded to the (220) crystal lattice plane of Fe. This conclusion is consistent with the finding of XRD powder analysis. Bright-field TEM micrographs show the cross-section of the electrowinning sample (Fig. 9(g)). The images revealed the stacking of polygonal sheets with clear boundaries and confirmed that the polygonal structure of the cluster cross-section was preserved well.

4. Conclusions

In this study, a novel and efficient method for the enhanced recovery of high-purity Fe powder from IREMR was proposed. The effects affecting the leaching and current efficiencies of Fe were systematically discussed. The findings indicate that when the mass ratio of H_2SO_4 to IREMR was 1:2.5 and the reaction temperature, current density, and elec-

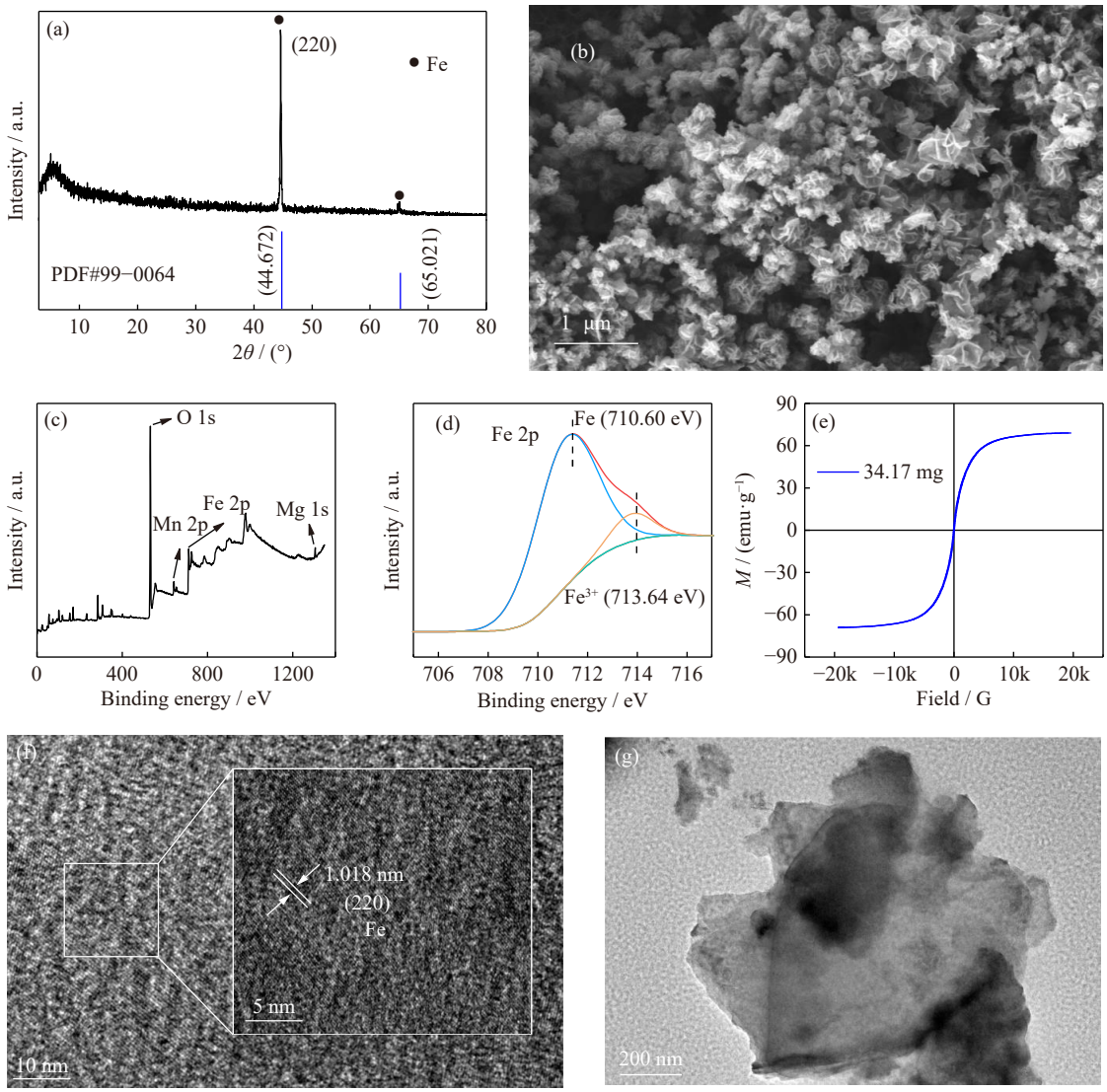

Fig. 9. XRD pattern (a), SEM image (b), XPS spectra (c, d), VSM (e), and TEM image (f), and bright-field TEM image (g) of the cathode electrowinning powder sample (temperature: 60°C, H_2SO_4 and IREMR mass ratio: 1:2.5; current density: 30 mA/cm^2; electrolytic time: 8 h).

trolytic time were 60°C, 30 mA/cm^2, and 8 h, respectively, the leaching efficiency, recovery efficiency, and purity of Fe were 92.58%, 80.65%, and 98.72wt%, respectively. The obtained electrolytic Fe powder had a high purity and desirable soft magnetic properties. This study has proposed a new strategy for IREMR resource utilization.

Acknowledgements

This work was financially supported by the Key Research and Development Program of Guangxi Province, China (No. AB23075174), the National Natural Science Foundation of China (No. 52174386), and the Science and Technology Plan Project of Sichuan Province, China (No. 2022YFS0459).

Conflict of Interest

All authors declare no conflict of interest.

References

[1] D.J. He, J.C. Shu, R. Wang, *et al*., A critical review on approaches for electrolytic manganese residue treatment and disposal technology: Reduction, pretreatment, and reuse, *J. Hazard. Mater.*, 418(2021), art. No. 126235.

[2] R.R. Zhang, X.T. Ma, X.X. Shen, *et al*., Life cycle assessment of electrolytic manganese metal production, *J. Clean. Prod.*, 253(2020), art. No. 119951.

[3] J.M. Lu, D. Dreisinger, and T. Glück, Electrolytic manganese metal production from manganese carbonate precipitate, *Hydrometallurgy*, 161(2016), p. 45.

[4] J.C. Shu, R.L. Liu, Z.H. Liu, H.L. Chen, and C.Y. Tao, Enhanced extraction of manganese from electrolytic manganese residue by electrochemical, *J. Electroanal. Chem.*, 780(2016), p. 32.

[5] M.G. Lei, B.Z. Ma, D.Y. Lv, C.Y. Wang, E. Asselin, and Y.Q. Chen, A process for beneficiation of low-grade manganese ore and synchronous preparation of calcium sulfate whiskers during hydrochloric acid regeneration, *Hydrometallurgy.*, 199(2021), art. No. 105533.

[6] S. Keshavarz, F. Faraji, F. Rashchi, and M. Mokmeli, Bioleaching of manganese from a low-grade pyrolusite ore using *Asper-*

gillus niger: Process optimization and kinetic studies, *J. Environ. Manage.*, 285(2021), art. No. 112153.
[7] J.C. Shu, R.L. Liu, Z.H. Liu, H.P. Wu, Y.L. Chen, and C.Y. Tao, Enhanced discharge performance of electrolytic manganese anode slime using calcination and pickling approach, *J. Electroanal. Chem.*, 806(2017), p. 15.
[8] Y.L. Deng, J.C. Shu, T.Y. Lei, X.F. Zeng, B. Li, and M.J. Chen, A green method for Mn^{2+} and NH_4^+–N removal in electrolytic manganese residue leachate by electric field and phosphorus ore flotation tailings, *Sep. Purif. Technol.*, 270(2021), art. No. 118820.
[9] B. Li, J.C. Shu, Y.H. Wu, *et al*., Enhanced removal of Mn^{2+} and NH_4^+–N in electrolytic manganese residue leachate by electrochemical and modified phosphate ore flotation tailings, *Sep. Purif. Technol.*, 291(2022), art. No. 120959.
[10] T.Y. Yang, Y. Xue, X.M. Liu, and Z.Q. Zhang, Solidification/stabilization and separation/extraction treatments of environmental hazardous components in electrolytic manganese residue: A review, *Process. Saf. Environ. Prot.*, 157(2022), p. 509.
[11] S.C. He, D.Y. Jiang, M.H. Hong, and Z.H. Liu, Hazard-free treatment and resource utilisation of electrolytic manganese residue: A review, *J. Clean. Prod.*, 306(2021), art. No. 127224.
[12] J. Li, Y.C. Liu, X. Ke, X.K. Jiao, R. Li, and C.J. Shi, Geopolymer synthesized from electrolytic manganese residue and lead-zinc smelting slag: Compressive strength and heavy metal immobilization, *Cem. Concr. Compos.*, 134(2022), art. No. 104806.
[13] D. Sun, L. Yang, N. Liu, *et al*., Sulfur resource recovery based on electrolytic manganese residue calcination and manganese oxide ore desulfurization for the clean production of electrolytic manganese, *Chin. J. Chem. Eng.*, 28(2020), No. 3, p. 864.
[14] D.Q. Wang, J.R. Fang, Q. Wang, and Y.J. Liu, Utilizing desulphurized electrolytic-manganese residue as a mineral admixture: A feasibility study, *Cem. Concr. Compos.*, 134(2022), art. No. 104822.
[15] P.X. Su, Q.Y. Wan, Y. Yang, *et al*., Hydroxylation of electrolytic manganese anode slime with EDTA-2Na and its adsorption of methylene blue, *Sep. Purif. Technol.*, 278(2021), art. No. 119526.
[16] J.Q. Wang, S.Y. Chen, X.F. Zeng, *et al*., Recovery of high purity copper from waste printed circuit boards of mobile phones by slurry electrolysis with ammonia-ammonium system, *Sep. Purif. Technol.*, 275(2021), art. No. 119180.
[17] K.X. Liu, S.Q. Huang, Y.X. Jin, L. Ma, W.X. Wang, and J.C.H. Lam, A green slurry electrolysis to recover valuable metals from waste printed circuit board (WPCB) in recyclable pH-neutral ethylene glycol, *J. Hazard. Mater.*, 433(2022), art. No. 128702.
[18] F.F. Li, M.J. Chen, J.C. Shu, *et al*., Copper and gold recovery from CPU sockets by one-step slurry electrolysis, *J. Clean. Prod.*, 213(2019), p. 673.
[19] J.T. Wu, B. Xu, Y.J. Zhou, Z.L. Dong, S.G. Zhong, and T. Jiang, A novel process of reverse flotation-hydrogen reduction for preparation of high-purity iron powder with superior magnetite concentrate, *Sep. Purif. Technol.*, 307(2023), art. No. 122784.
[20] D. Chen, S. Chen, H.W. Guo, *et al*., A novel metallurgical technique for the preparation of soft magnetic iron carbide from low-grade siderite, *J. Alloys Compd.*, 928(2022), art. No. 167186.
[21] S. Iimura, T. Sasaki, K. Hanzawa, S. Matsuishi, and H. Hosono, High pressure synthesis, physical properties and electronic structure of monovalent iron compound LaFePH, *J. Solid State Chem.*, 315(2022), art. No. 123546.
[22] J.L. Lv and H.Y. Luo, The effects of cold rolling temperature on corrosion resistance of pure iron, *Appl. Surf. Sci.*, 317(2014), p. 125.
[23] L. Khan, K. Sato, S. Okuyama, *et al*., Ultra-high-purity iron is a novel and very compatible biomaterial, *J. Mech. Behav. Biomed. Mater.*, 106(2020), art. No. 103744.
[24] J. Qiu, J. Han, R. Schoell, *et al*., Electrical properties of thermal oxide scales on pure iron in liquid lead-bismuth eutectic, *Corros. Sci.*, 176(2020), art. No. 109052.
[25] H. Matsumiya, T. Kato, and M. Hiraide, Ionic liquid-based extraction followed by graphite-furnace atomic absorption spectrometry for the determination of trace heavy metals in high-purity iron metal, *Talanta.*, 119(2014), p. 505.
[26] Q. Liang, J.Q. Wang, S.Y. Chen, *et al*., Electrolyte circulation: Metal recovery from waste printed circuit boards of mobile phones by alkaline slurry electrolysis, *J. Clean. Prod.*, 409(2023), art. No. 137223.
[27] J.Q. Wang, Z.M. Huang, D.Z. Yang, *et al*., A semi-scaled experiment for metals separating and recovering from waste printed circuit boards by slurry electrolysis, *Process. Saf. Environ. Prot.*, 147(2021), p. 37.
[28] Y.X. Zhao, M.M. Sun, Y.L. Zhang, Y.Z. Zhao, and H.H. Ge, Efficient and rapid electrocatalytic degradation of polyethylene glycol by ammonium jarosite, *J. Environ. Chem. Eng.*, 10(2022), No. 3, art. No. 107795.
[29] J.L. Yang, J.G. Liu, H.X. Xiao, and S.J. Ma, Sulfuric acid leaching of high iron-bearing zinc calcine, *Int. J. Miner. Metall. Mater.*, 24(2017), No. 11, p. 1211.
[30] B.J. Wang, L.L. Mu, S. Guo, and Y.F. Bi, Lead leaching mechanism and kinetics in electrolytic manganese anode slime, *Hydrometallurgy.*, 183(2019), p. 98.
[31] T.Y. Lei, J.C. Shu, Y.L. Deng, *et al*., Enhanced recovery of copper from reclaimed copper smelting fly ash via leaching and electrowinning processes, *Sep. Purif. Technol.*, 273(2021), art. No. 118943.
[32] J.M. Gao, B. Wang, W.J. Li, L. Cui, Y.X. Guo, and F.Q. Cheng, High-efficiency leaching of Al and Fe from fly ash for preparation of polymeric aluminum ferric chloride sulfate coagulant for wastewater treatment, *Sep. Purif. Technol.*, 306(2023), art. No. 122545.
[33] Y.G. Zhang, M.J. Chen, Q.X. Tan, B. Wang, and S. Chen, Recovery of copper from WPCBs using slurry electrolysis with ionic liquid $[BSO_3HPy]\cdot HSO_4$, *Hydrometallurgy.*, 175(2018), p. 150.
[34] E. Demircilioğlu, E. Teomete, E. Schlangen, and F.J. Baeza, Temperature and moisture effects on electrical resistance and strain sensitivity of smart concrete, *Constr. Build. Mater.*, 224(2019), p. 420.
[35] R. Kallio, U. Lassi, T. Kauppinen, *et al*., Leaching characteristics of Sc-enriched, Fe-depleted acidic slags, *Miner. Eng.*, 189(2022), art. No. 107901.
[36] B. Miranda-Alcántara, F. Castañeda-Záldivar, L. Ortíz-Frade, R. Antaño, and F.F. Rivera, Electrochemical study of iron deposit in acid media for its recovery from spent pickling baths regeneration, *J. Electroanal. Chem.*, 901(2021), art. No. 115805.
[37] M.C. Nolasco, L.F. Flores, E.J. Gutiérrez, *et al*., Acid dissolution of jarosite-type compounds: Effect of the incorporation of divalent cations into the structure on the reaction rate, *Hydrometallurgy.*, 212(2022), art. No. 105907.
[38] Y. Shi, K.X. Jiang, T.A. Zhang, and X.F. Zhu, Electrolysis designed for clean production of selective iron products from coal fly ash leachate, *Hydrometallurgy.*, 203(2021), art. No. 105617.
[39] P.F. Liu and Y.F. Zhang, Crystallization of ammonium jarosite from ammonium ferric sulfate solutions, *Hydrometallurgy.*, 189(2019), art. No. 105133.
[40] J.C. Shu, H.P. Wu, M.J. Chen, *et al*., Simultaneous optimizing removal of manganese and ammonia nitrogen from electrolytic metal manganese residue leachate using chemical equilibrium model, *Ecotoxicol. Environ. Saf.*, 172(2019), p. 273.
[41] M. Ristić, S. Musić, and Z. Orehovec, Thermal decomposition of synthetic ammonium jarosite, *J. Mol. Struct.*, 744-747(2005), p. 295.